

Parameter extraction for a superconducting thermal switch (hTron) SPICE model

Valentin Karam^{1*}, Owen Medeiros¹, Tareq El Dandachi¹, Matteo Castellani¹,
Reed Foster¹, Marco Colangelo¹, Karl Berggren¹

¹Department of Electrical Engineering and Computer Science, Massachusetts Institute of Technology, 77 Massachusetts Ave., Cambridge, 02139, Massachusetts, USA.

*Corresponding author(s). E-mail(s): vkaram@mit.edu;

Abstract

Efficiently simulating large circuits is crucial for the broader use of superconducting nanowire-based electronics. However, current simulation tools for this technology are not adapted to the scaling of circuit size and complexity. We focus on the multilayered heater-nanocryotron (hTron), a promising superconducting nanowire-based switch used in applications such as superconducting nanowire single-photon detector (SNSPD) readout. Previously, the hTron was modeled using traditional finite-element methods (FEM), which fall short in simulating systems at a larger scale. An empirical-based method would be better adapted to this task, enhancing both simulation speed and agreement with experimental data.

In this work, we perform switching current and activation delay measurements on 17 hTron devices. We then develop a method for extracting physical fitting parameters used to characterize the devices. We build a SPICE behavioral model that reproduces the static and transient device behavior using these parameters, and validate it by comparing its performance to the model developed in a prior work, showing an improvement in simulation time by several orders of magnitude. Our model provides circuit designers with a tool to help understand the hTron's behavior during all design stages, thus promoting broader use of the hTron across various new areas of application.

Keywords: superconducting, nanowire, heater-Tron, hTron, SPICE, model, cryotron

1 Introduction

The field of superconducting electronics has demonstrated significant benefits in areas such as quantum computing [1], imaging [2], neuromorphic computing [3], and digital logic [4]. Josephson junction (JJ)-based circuits dominate the field, thanks to their fast operation speeds and low power dissipation [5].

However, JJs have low signals, low normal resistance, and are sensitive to magnetic fields. In contrast, superconducting nanowires can operate in noisy environments, offer high gains and exhibit high impedance and fan-out [6–8]. Therefore, they present a complementary device to JJs for certain applications. In particular, the capability of nanowire-based circuits to drive high loads makes them compatible with complementary metal-oxide-semiconductor (CMOS) technologies [9–11].

Multiple nanowire-based devices have been introduced in the past, such as the nanocryotron (nTron) [6] and the heater-nanocryotron (hTron) [12]. The nTron is a three-terminal device that uses a constriction at the gate input to suppress a superconducting channel. It has a maximum demonstrated clock frequency of 615.4 MHz [13], but suffers from leakage current between the gate and channel. The hTron device — in its multiplanar version — uses the Joule heating from a normal heater to suppress a superconducting channel deposited beneath it. An oxide layer separates the heater layer from the superconducting layer, which isolates the layers galvanically while coupling them thermally. The hTron is easier to fabricate than the nTron due to the absence of constriction, and does not present the issue of leakage currents [12].

These two nanowire-based devices allowed the creation of a logic family [14], a memory cell [15], and are particularly used in Superconducting nanowire single-photon detector (SNSPD) arrays, both for pulse amplification and readout [16–19]. The nTron can also be used to translate SFQ pulses to CMOS [9]. When a higher impedance is needed, an nTron and hTron can be combined in an amplification stage, *e.g.*, to drive an LED and communicate between superconducting neurons [20, 21]. If used in larger and more complex circuits, superconducting nanowires thus have the potential to complement Josephson junctions (JJs) and thus enable new superconducting electronics applications.

However, the scaling of these nanowire-based circuits is currently limited to a few devices per circuit [18, 19]. We can partly explain this deficiency by the lack of simulation tools for superconducting nanowires, which is crucial to their development. Baghdadi et al. developed a 3D electrothermal model for the hTron using finite-element modeling (FEM) techniques, modeling heat exchanges inside the device by solving differential heat equations [12]. This model, while helpful at the device level

during early development stages, cannot easily simulate large-scale circuits, mainly because of the differential equations stiffness and the difference of scales in the geometry of these layered devices. A simpler, less accurate 0D model has also been developed, which was implemented in SPICE [21]. However, this simpler model is slow to solve, and suffers from convergence issues. Moreover, both models suffer from a lack of agreement with experimental data. Indeed, the heat equations require various physical parameters to be approximated from literature or experiment [12]. This means that the model has to be tuned and optimized each time the geometry is changed. An arbitrary heater and channel widths cannot simply be plugged in to get a nice agreement with measurements, because many of the material's thermal parameters are geometry-dependent (*e.g.*, boundary resistance or diffusion coefficient).

These issues can be solved by developing a physics-informed behavioral model. Instead of focusing on the device's microscopic physics and heat exchanges, behavioral models fit experimental data using a minimal set of parameters. This approach allows physics-informed behavioral models to be more simple due to their empirical basis, while also being robust thanks to fitting equations arising from phenomenological physics.

More precisely, we can divide the hTron response to a given heater current into a static and a transient response. The static response is defined by the channel switching current, whereas the device activation delay — delay between the input of a heater pulse and the channel switching — leads to the modeling of the transient response. To model the hTron behavior, the critical current and activation delay dependence on heater current have to be measured.

In this paper, we characterize 17 hTron devices from a single wafer and explain their static behavior using only two physical parameters. We introduce a systematic approach to extract these parameters from measurements of critical current as a function of heater current. Furthermore, we demonstrate the correlation of these parameters with the heater and channel widths. The transient response of the device, which depends on the heat flow from the heater to the channel through the oxide layer, is also modeled to fit experiments, allowing us to accurately simulate the device close to the maximum operating speed. Finally, we assess the simulation speed and accuracy of our method, comparing it to the previous electrothermal model by applying our parameter extraction method on measurement data from the previous hTron study [12]. We achieve improved agreements with published experimental data and successfully replicate published results. Moreover, our simulation time is lower by several order of magnitude, making our approach compatible for use by circuit

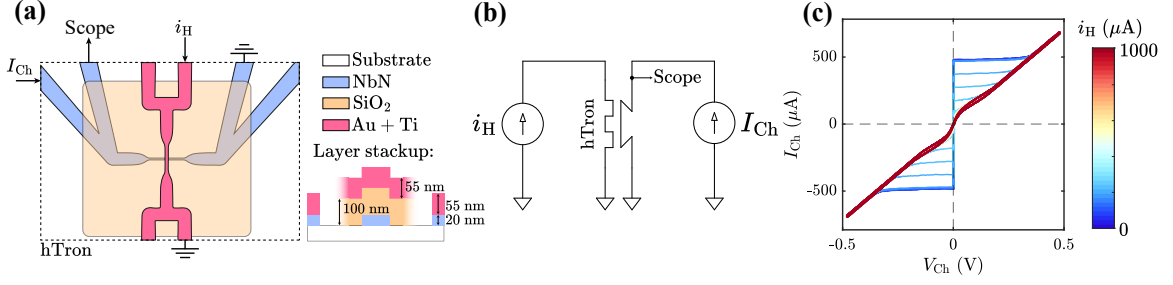


Fig. 1: Device geometry and typical circuit

a) Device geometry, layers stackup, and typical circuit to perform I-V measurements using the 4-points measurement, which is further detailed on the b) schematics. c) I-V curve showing the influence of heater current on the switching current.

designers. This novel behavioral model is a first step into a broader use of superconducting nanowire-based devices in more complex circuits.

2 Methods

In this section, we outline our methodological approach to constructing, characterizing and modeling hTron devices. First, we delve into the fabrication techniques. Following this, we explain the electrical measurement procedures applied to the hTron devices, providing insights into their functional characteristics. Lastly, we describe our modeling techniques, including the specifics of our SPICE implementation.

2.1 Fabrication

Here we present the hTron fabrication process we used, which is comparable to the one introduced by Baghdadi et al [12]. The Figure 1a depicts the device layout together with the layer stackup.

The hTron fabrication process starts with the deposition of a uniform layer of Niobium nitride (NbN) layer with thickness $d_c = 20$ nm onto a silicon substrate using RF-biased sputtering [22]. Subsequently, 5 nm Ti and 50 nm Au were deposited with a liftoff process to pattern the pads, that serve as wire-bonding connections for the hTron ports. Following this, the channel is patterned into the underlying NbN layer with electron beam lithography (EBL) followed by reactive ion etching. A 100 nm silicon oxide layer is deposited using a PECVD technique to isolate the heater and channel layers. Finally, the heaters are patterned with another liftoff process using the same Ti/Au thickness ratio.

In total, 9 distinct geometry combinations were patterned on two 10×10 mm dies from a single wafer. The nanowire configurations varied in heater width w_h and channel width w_c of 100 nm,

500 nm, and 1 μm , and all had lengths of 10 μm . However, one device with $w_h = 100 \text{ nm}$ and $w_c = 1 \mu\text{m}$ was damaged while measuring, resulting in a total of 17 functional devices. As seen in Figure 1a, each terminal of the hTron is connected to 2 different pads, known as a 4-point measurement setup.

2.2 Measurement Setup

This section details the experimental setup used to measure the relation between switching current I_{SW} as a function of the heater current i_h , $I_{\text{SW}}(i_h)$, as shown in Figure 1a and Figure 1b. This relation explains the steady-state behavior of the hTron device. For our experiments, we used an immersion probe inside a liquid helium dewar [23], setting a substrate temperature of $T_{\text{SUB}} = 4.2 \text{ K}$.

The switching current is determined by gradually sweeping the channel current both positively and negatively using an arbitrary waveform generator (AWG) until the device switches in the resistive state, resulting in a detectable voltage. The AWG waveform frequency is set to 10 kHz so that the period would be much larger than the hotspot growth time. We record the voltage as close to the channel as possible using the 4-points setup. The dependence of the switching current on the heater current is then obtained by biasing the heater with a DC current i_h while performing the channel sweep. A typical result is shown as a current-voltage (I-V) plot in Figure 1c, where we can see the switching current being gradually lowered by the increase of heater current. For high heater currents, the channel temperature approaches T_C , and thus the channel is fully suppressed. To compensate for the intrinsic stochastic nature of the switching characteristics of the devices, each datapoint is the result of an average of 100 trials [24].

The channel switching current can also be modulated by increasing the entire substrate temperature. To characterize this effect, we used a commercial temperature controller with a heater located inside the immersion probe itself. By doing so, the whole sample is globally heated, allowing the characterization of the direct dependence between the channel's switching current and temperature.

To conclude, the evolution of the switching current was characterized as a function of the substrate temperature and heater current. Both measurements highlight different components of the device behavior. Throughout this paper, we use the switching current density $J_{\text{SW}} = I_{\text{SW}}/(w_c \cdot d_c)$ instead of the switching current, making our measurements independent on the channel width.

2.3 Modeling

This subsection presents our approach to modeling the hTron device, focusing on developing a behavioral model grounded in empirical data. We describe the fitting functions and parameters, which are critical for accurately replicating and predicting the hTron device's behavior.

2.3.1 Physics-informed behavioral model

We developed a physics-informed behavioral model based on a set of equations and fitting parameters to fit the $I_{SW}(i_H)$ experimental data that we collected. In our approach, we treat the hTron as a four-terminal black-box, focusing on modeling its behavior rather than its intricate physical properties, which we consider unknown.

The fitting parameters can typically vary from one device to another, and across two devices with same geometry. However, we found correlations between the fitting parameters and the device's widths (w_c and w_h), allowing us to predict the behavior of a device from its geometry.

2.3.2 Fitting functions

We translated the flow of events governing the hTron static behavior by using two analytical expressions, the first one estimating the channel temperature from a heater current input, and the second one predicting the switching current at this temperature.

First we estimate the channel temperature from the heater current:

$$t_{Ch}(i_H) = \left[(T_C^4 - T_{SUB}^4) \cdot \left(\frac{i_H}{I_{H,SUPP}} \right)^\eta + T_{SUB}^4 \right]^{\frac{1}{4}} \quad (1)$$

$I_{H,SUPP}$ is the suppressing current — the heater current at which the channel is fully suppressed and reaches the critical temperature T_C . The parameter η is the strength of the thermal dependence between the heater current and the estimated channel temperature. While we used $\eta = 2$ in our model, its value will be discussed in Section 5.

We then find the unconstricted switching current density from the estimated channel temperature, $\hat{J}_{SW}(t_{Ch})$, defined as the switching current density of the channel section located immediately below the heater:

$$\widehat{J}_{\text{SW}}(t_{\text{Ch}}) = \widehat{J}_{\text{C}} \cdot \left[1 - \left(\frac{t_{\text{Ch}}}{T_{\text{C}}} \right)^3 \right]^{2.1}, \quad t_{\text{Ch}} \leq T_{\text{C}}$$

$$\text{with } \widehat{J}_{\text{C}} = \frac{\widehat{J}_{\text{SW}}(T_{\text{SUB}})}{\left[1 - \left(\frac{T_{\text{SUB}}}{T_{\text{C}}} \right)^3 \right]^{2.1}} \quad (2)$$

This function was introduced in [12]. The parameter \widehat{J}_{C} is the channel's unconstricted critical current density, *i.e.*, the switching current at zero Kelvin of the channel section located immediately below the heater. It can be obtained directly from $\widehat{J}_{\text{SW}}(T_{\text{SUB}})$, the unconstricted switching current density at substrate temperature.

By combining these two simple functions in the form $\widehat{J}_{\text{SW}}(t_{\text{Ch}}(i_{\text{H}})) = \widehat{J}_{\text{SW}}(i_{\text{H}})$, we were able to accurately fit our measurement data $J_{\text{SW}}(i_{\text{H}})$. The fitting parameters $\widehat{J}_{\text{SW}}(T_{\text{SUB}})$ and $I_{\text{H,SUPP}}$ are extracted from measurements.

$$\widehat{J}_{\text{SW}}(i_{\text{H}}) = \widehat{J}_{\text{C}} \cdot \left[1 - \left(\frac{1}{T_{\text{C}}} \cdot \left[(T_{\text{C}}^4 - T_{\text{SUB}}^4) \cdot \left(\frac{i_{\text{H}}}{I_{\text{H,SUPP}}} \right)^\eta + T_{\text{SUB}}^4 \right]^{\frac{1}{4}} \right)^3 \right]^{2.1} \quad (3)$$

This equation models the switching current density of the channel portion located directly below the heater. However, at low heater current the devices often exhibit a constant switching current, or plateau. This plateau suggests a defect or constriction along the channel in an area distant from the heater (as detailed in Section 3: Results). In that case, the measured switching current density at substrate temperature will differ from $\widehat{J}_{\text{SW}}(T_{\text{SUB}})$. To match these observations, the model switching current density can be rewritten as:

$$J_{\text{MODEL}}(i_{\text{H}}) = \min \left\{ \widehat{J}_{\text{SW}}(i_{\text{H}}), J_{\text{CONSTR}} \right\}, \quad J_{\text{CONSTR}} \leq \widehat{J}_{\text{SW}}(T_{\text{SUB}}) \quad (4)$$

The value J_{CONSTR} is the measured switching current when the heater current is zero. In practice, it is equal to the measured switching current density at substrate temperature, $J_{\text{SW}}(T_{\text{SUB}})$. A value of $J_{\text{CONSTR}} = \widehat{J}_{\text{SW}}(T_{\text{SUB}})$ would mean no plateau is observed. In practice, most of the measured devices present a plateau at low heater currents.

2.4 SPICE Implementation

In this subsection we describe the steps undertaken to build the simulation model in SPICE [25], thus enabling the use of the modeled hTron device in circuits. The SPICE model file is available in the supplementary material.

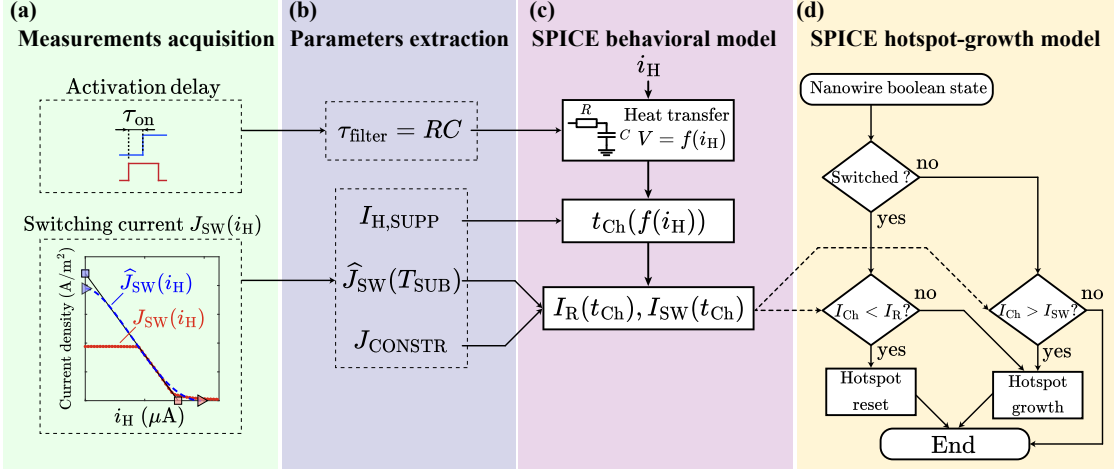


Fig. 2: End-to-end process for the hTron SPICE modeling.

a) Activation delay measurements allow to retrieve the transient device response, and heater current-dependent switching current measurements define the static device response. **b)** The heat transfer time constant τ_{filter} is computed from the activation delay. The fitting parameters $I_{\text{H,SUPP}}$ and $\hat{J}_{\text{SW}}(T_{\text{SUB}})$, together with the plateau level J_{CONSTR} are extracted from $J_{\text{SW}}(i_{\text{H}})$ curves. **c)** The fitting parameters are further fed into SPICE, computing the nanowire temperature, switching current, and retrapping current at each simulation time step thanks to the according fitting functions. The heat transfer through the oxide layer is simulated by a lumped-element RC circuit, giving rise to a delay in the hTron response to an input heater pulse. **d)** The switching and retrapping current are finally used to define the hotspot behavior, that is either growing or retrapping depending on the current flowing in the channel I_{Ch} . The device geometry and NbN resistance define the hotspot growth rate and normal resistance.

When a particular device with channel width w_c and heater width w_h is to be characterized, the device geometry and wafer material properties are gathered prior to performing electrical measurements. The NbN thickness are measured using an ellipsometer [26], and the widths and lengths are measured from scanning electron micrographs. The NbN sheet resistance, which is used by the hotspot growth model, is also acquired. The steps showing the building of a SPICE model from the electrical characterization of a device are schematically represented in Figure 2.

In a first step (Figure 2a), electrical measurements must be performed. The activation delay τ_{on} (delay between the input of a heater pulse and the channel switching) is measured to further define the transient behavior of the device. The heater current-dependent switching current density $J_{\text{SW}}(i_{\text{H}})$ is also measured to set the static device behavior.

Subsequently (Figure 2b), the time constant of the heat transfer sub-circuit τ_{filter} , the suppressing current $I_{\text{H,SUPP}}$, the unconstricted switching current at substrate temperature $\hat{J}_{\text{SW}}(T_{\text{SUB}})$, and the plateau level J_{CONSTR} are extracted from the measurement data. Specifically, τ_{filter} is directly

computed from τ_{on} , and $I_{\text{H,SUPP}}$, $\hat{J}_{\text{SW}}(T_{\text{SUB}})$, and J_{CONSTR} are obtained from $J_{\text{SW}}(i_{\text{H}})$ curves using the method detailed in Section 3 : Results.

In a third step (Figure 2c), the SPICE behavioral model uses the fitting parameters to compute the switching current I_{SW} and retrapping current I_{R} from a heater current input. The temporal behavior of the heat transfer between the heater and the NbN layer through the oxide is modeled using a simple heat transfer circuit with lumped elements (low-pass filter), which time constant is $RC = \tau_{\text{filter}}$. Without this added sub-circuit, the temperature of the nanowire would start to grow instantaneously with a heater current input, which does not reflect real observations. The exact computation of τ_{filter} can be found in the supplementary material.

The channel temperature and switching current are then computed using expression-based functions defined using the `.func` SPICE directive. This directive computes the value of a custom expression without the need of adding a voltage node, and a SPICE behavioral source allows one to probe the value of the function. Due to the low computational cost and analytical nature of the fitting functions, the SPICE implementation of our fitting functions is a straight-forward process. This simplicity is an asset, as the solver updates the temperature, switching current and retrapping current at each time step, in response to the input heater current.

Finally, the channel current is compared to the switching and retrapping currents to compute the hotspot resistance (Figure 2d). A channel current above the switching current threshold would induce hotspot growth, after which it would eventually reset by decreasing below the retrapping current. The SPICE model of the non-linear inductor and hotspot behavior was based on the superconducting nanowire SPICE model introduced by Berggren et al. [27], however, the model was modified to embed a hotspot growth circuit based on the built-in SPICE integrator function `sdt()`. The work by El Dandachi [28] has proven this new approach to present multiple benefits over the previous nanowire SPICE model.

3 Results

In this chapter we present the results of our research, going through the fabrication, the devices characterization and the model design. We will further analyze the model parameters and explain their dependence in device geometry. Finally, we will compare the simulations and measurements of the device activation delay.

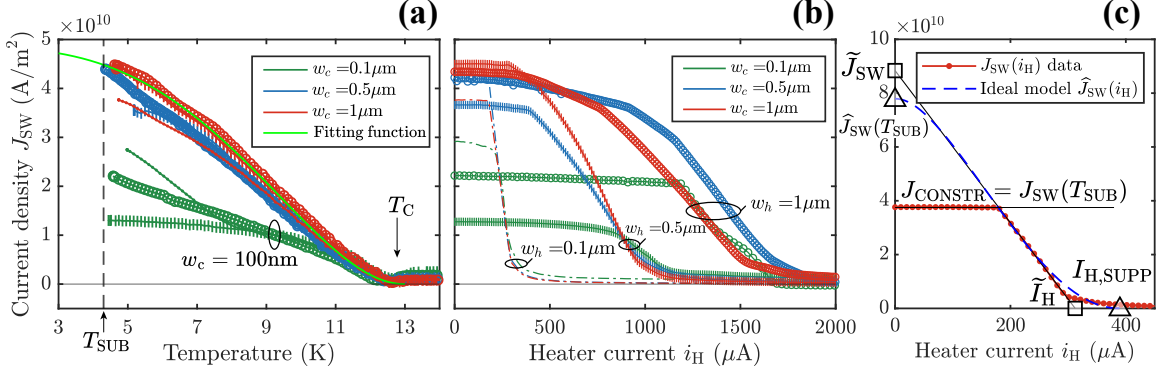


Fig. 3: Measurement results and method for extracting model parameters

Experimental data of the switching current density of 9 different hTron geometries, plotted against **a**) the substrate temperature and against **b**) the heater current. Equation 2 was fitted to one of the data curves, showing a smooth transition from T_{SUB} to T_C . Heater-dependent switching current curves show a plateau at low heater currents, indicating that the heater current does not modulate the channel switching current. **c)** Method developed to extract the model parameters from $J_{SW}(i_H)$ measurement plots. A line is fitted to the linear part of the measurement data, which sets the non-physical fitting parameters \tilde{I}_H and \tilde{J}_{SW} (indicated by \square). The suppressing current $I_{H,SUPP}$ and the unconstricted switching current at substrate temperature $\hat{J}_{SW}(T_{SUB})$ (indicated by \triangle), that define the unconstricted model $\hat{J}_{SW}(i_H)$, are further derived from the non-physical parameters. In this example, a constriction strongly limits the switching current of the measured device at low heater current, but can be taken into account by defining $J_{MODEL}(i_H) = \min\{\hat{J}_{SW}(i_H), J_{CONSTR}\}$.

3.1 Fabrication results

The deposited NbN film shows a critical temperature of $T_C \simeq 12.5\text{ K}$, a thickness — measured with ellipsometry — of $d_c = 23.6\text{ nm}$ and a sheet resistance of $R_{SHEET} = 77.9\Omega/\square$. The length of the channel and heater strips is $l_c = l_h = 10\mu\text{m}$. Using these parameters, a depairing current of $J_{dep} = 16.44 \times 10^{10}\text{ A/m}^2$ was computed using the Equation 13 of Charaev et al [29]. Heater resistances of 44.2Ω , 10.4Ω , and 7.2Ω were measured on devices with heaters widths of $0.1\mu\text{m}$, $0.5\mu\text{m}$, and $1\mu\text{m}$ respectively, however, device-to-device variations are likely to be observed. The heater resistance could be engineered by tuning the heater length, which would not impair the device operation. However, power is wasted to the substrate if the heater length is greater than the channel width.

3.2 Device characterization

As shown on Figure 3a, the channel switching current density of measured devices is smoothly reduced with temperature, until the channel is fully suppressed at $T_C \simeq 12.5\text{ K}$. Moreover, the experimental data agrees nicely with the fitting function $J_{SW}(T) = 4.48 \times 10^{10} \cdot \left(1 - (T/T_C)^3\right)^{2.1} [\text{A/m}^2]$, that was fitted to a particular measurement curve. All other curves are thus expected to disagree with this fit.

On the other hand, Figure 3b shows the switching current density's dependence on heater current. This plot is used to extract the two fitting parameters $\hat{J}_{\text{SW}}(T_{\text{SUB}})$ and $I_{\text{H,SUPP}}$, together with the additional value J_{CONSTR} . Two comments can be made on this plot : (1) a plateau appears for low heater currents, and (2) the suppressing current is correlated to the heater width but not to the channel width. These observations are discussed in Section 3.4 and Section 3.5, respectively.

3.3 Parameter Extraction

Here we explain the developed step-by-step method to extract the two model parameters from a particular $J_{\text{SW}}(i_{\text{H}})$ measurement curve, represented schematically with a typical measurement curve on Figure 3c. The key idea is to recover the measurements that would have been observed if the constriction outside the heated area (*i.e.*, the plateau) would not have been there. To do so, we used the information contained in the linear part of the $J_{\text{SW}}(i_{\text{H}})$ measurement data:

1. Fit a straight line to the linear part of the curve, ignoring the plateau on the left side and the part on the right side (where the switching current reaches zero).
2. This linear fit defines \tilde{J}_{SW} and \tilde{I}_{H} , the intersection between the line and the y and x axis, respectively.
3. The fitting parameters can be recovered : $\hat{J}_{\text{SW}}(T_{\text{SUB}}) = \alpha \cdot \tilde{J}_{\text{SW}}$, and $I_{\text{H,SUPP}} = \beta \cdot \tilde{I}_{\text{H}}$. The α and β constants are correction parameters obtained by fitting a straight line to the fitting function directly. These constants simply account for the fitting function's curvature, and are valid for a same value of η . We found $\alpha = 0.88$ and $\beta = 1.25$ for $\eta = 2$. Plugging $I_{\text{H,SUPP}}$ into Equation 1 and $\hat{J}_{\text{SW}}(T_{\text{SUB}})$ into Equation 2 gives the unconstricted model $\hat{J}_{\text{SW}}(i_{\text{H}})$ as defined in Equation 3, which represents the measurement we would observe if there was no plateau.
4. The final model expression — including the plateau — is defined in Equation 4: $J_{\text{MODEL}}(i_{\text{H}}) = \min\{\hat{J}_{\text{SW}}(i_{\text{H}}), J_{\text{CONSTR}}\}$, the minimum between the unconstricted model $\hat{J}_{\text{SW}}(i_{\text{H}})$ and the constriction level J_{CONSTR} . Any J_{CONSTR} value can be set in order to set various constriction levels, depending on the application.

3.4 Analysis of constrictions outside of the heated area

The presence of a plateau at low heater current in Figure 3b suggests that most devices' switching currents are limited by one or multiple weak spots located along the channel, away from the heated area. At low heater currents, these weak spots switch at lower channel currents than the channel portion below the heater. We therefore observe a lower switching current than that of the heated

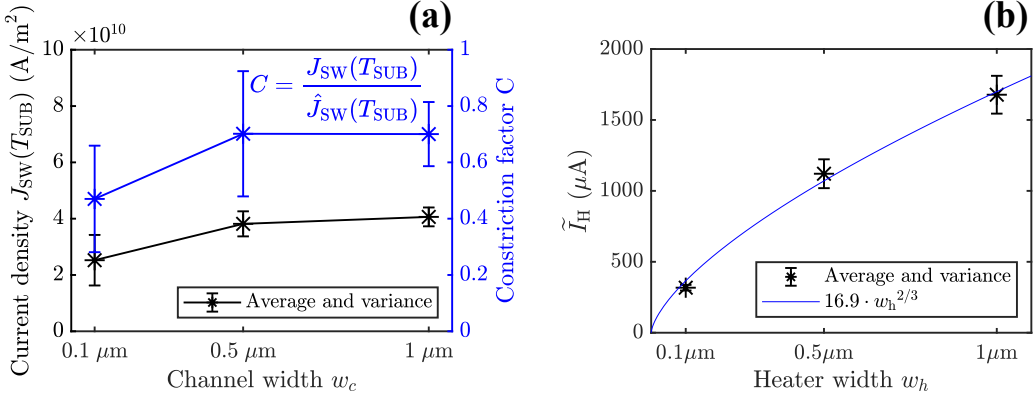


Fig. 4: Results analysis: prediction of the model parameters

a) In black: measured switching current density at substrate temperature $J_{SW}(T_{SUB})$ (which can be seen in the form of a plateau) against the device channel width. In blue: constriction factor C , defined as the measured critical current density divided by the predicted switching current density. The average constriction factor is similar for $w_c = 1 \mu\text{m}$ and $0.5 \mu\text{m}$ but decreases significantly for $w_c = 0.1 \mu\text{m}$. b) Predicted fitting parameter \tilde{I}_H dependence on the heater width, with a power-law fit. For both plots, each point is an average over all device with indicated heater or channel width.

region. As the heater current increases, a point is reached where the heated part of the channel starts to switch at a current lower than that of the weak spot. This marks a significant change, as the plateau abruptly collapses. Beyond this point, with further increases in heater current, the switching occurs directly under the heater, where the switching current is at its minimum. This process continues until the channel is completely suppressed.

Constrictions are common candidates for weak spots in superconducting nanowires [30]. In Figure 4a (in black), we plotted the switching current density of the weak spot $J_{SW}(T_{SUB})$ against the channel width. It can be seen that the switching current density of the weak spot is similar for $1 \mu\text{m}$ -wide channels and $0.5 \mu\text{m}$ -wide channels, but decreases significantly for $0.1 \mu\text{m}$ -wide channels, while also showing greater variance. The same trend can also be seen with the constriction factor C , plotted in blue, defined as the ratio between the measured switching current at substrate temperature $J_{SW}(T_{SUB})$ and the ideal predicted critical current at substrate temperature $\hat{J}_{SW}(T_{SUB})$. The fact that the devices with the narrowest channels are more constricted would potentially result from the channel line-width roughness, which degrades as the width decreases [31].

Finally, if our fabrication process was perfect, $\hat{J}_{SW}(T_{SUB})$ should in theory be the same for all devices from a same wafer, and should not depend on the channel width. In practice, despite some variance, the average $\hat{J}_{SW}(T_{SUB})$ value is indeed comparable across devices with different channel widths. This would imply that the channel's average switching current density is similar among devices, despite showing localised constrictions.

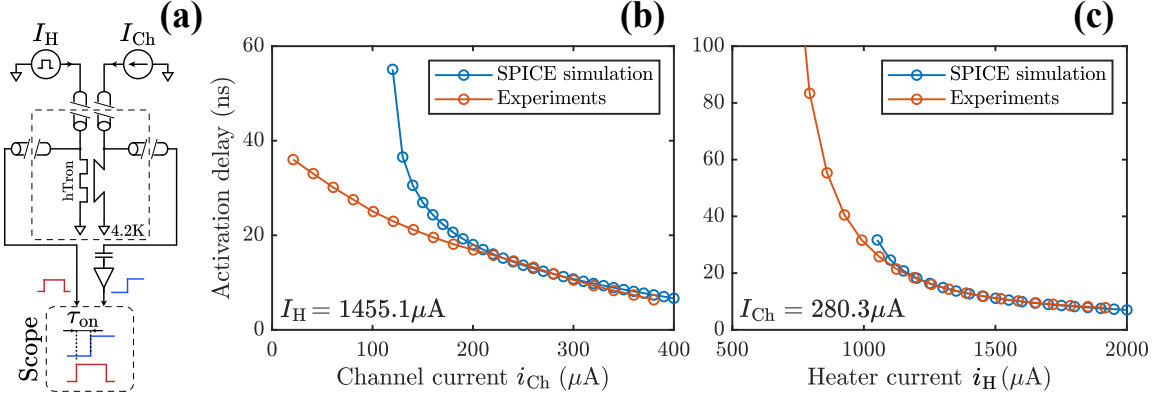


Fig. 5: Prediction of the hTron maximum operating speed

a) Simplified schematics of the measurement setup of the hTron activation delay τ_{on} , defined as the channel response time following the application of a heater current pulse of magnitude I_{H} . The heater current pulse duration is much larger than τ_{on} . We plotted the measured and simulated activation delay against b) the channel bias current (for a constant heater current), and c) the heater current amplitude (for a constant channel current). The graphs highlight the model's predictive capability across a large span of input currents, despite a deviation from actual measurements at lower current levels, due the simplicity of our heat transfer model. The device heater width and channel width are 1 μm and 0.5 μm , respectively.

3.5 Analysis and prediction of the suppressing current

The suppressing current parameter $I_{\text{H,SUPP}}$ has smaller values for narrower heaters, and can be expressed as a function of the heater width w_{h} , as shown in Figure 4b. The function $\tilde{I}_{\text{H}}(w_{\text{h}}) = 16.9 \cdot w_{\text{h}}^{2/3}$, resulting from a power-law fitting, predicts the suppressing current for different heater widths. As reducing w_{h} increases both the resistance and the dissipated power per unit area, the suppressing current decreases faster for narrower heaters. Here, the fitting parameter, valid for an entire wafer, embeds information about the oxide thickness and heater's materials properties.

3.6 hTron maximum operating speed

The transient response of the hTron is defined by the heat transfer from the heater to the channel through the oxide. It limits the operating speed of the hTron devices, resulting in a non-zero device activation delay, τ_{on} . This delay, measured as the time needed to observe a channel switch after the input of a heater pulse, is a key aspect of the device behavior.

In Figure 5a, we show the measurement setup used to measure the activation delay τ_{on} at a specific $(I_{\text{H}}, I_{\text{Ch}})$ operating point. The results of sweeping the channel current while maintaining a fixed heater current are shown in Figure 5b. Figure 5c illustrates the results when the heater current is varied with a fixed channel current. In order to reproduce this data in SPICE, we first choose an operating point ($I_{\text{H}} = 1455.1 \mu\text{A}$, $I_{\text{Ch}} = 280.3 \mu\text{A}$), and extract the activation delay from

the experiments ($\tau_{\text{on}} = 11.85 \text{ ns}$). We further obtain the RC time constant of our heat transfer sub-circuit to $RC = \tau_{\text{filter}} = 10.0 \text{ ns}$ directly from the activation delay value (details can be found in the supplementary material). Sweeping the input currents in the same way in SPICE as we did in the experiments, we observe that the model is reliable around the operating point ($I_H = 1455.1 \mu\text{A}$, $I_{\text{Ch}} = 280.3 \mu\text{A}$) and for high currents.

This simple and efficient method allowed us to simulate the temporal behavior of the hTron device, and can be used to determine the maximum operating speed in real circuits. While the model diverges from the measurements at low currents, the accuracy of this result could be improved with added degrees of freedom in the heat transfer sub-circuit.

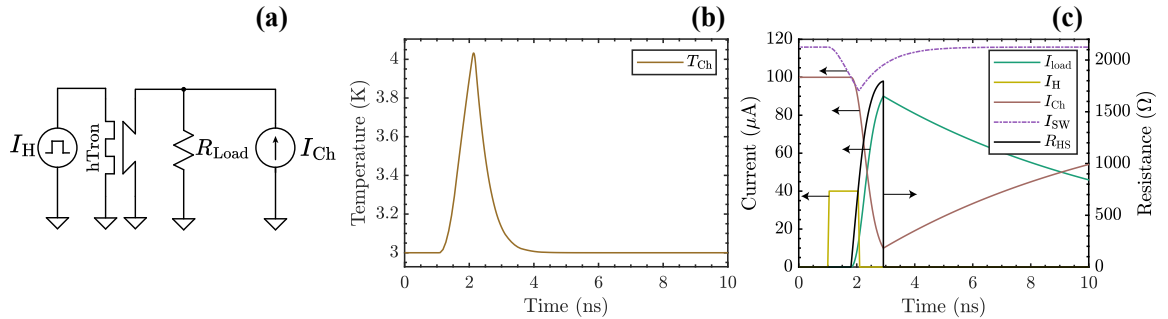


Fig. 6: Reproduction of Baghdadi et al. [12] results from an $I_{\text{SW}}(i_H)$ measurement.

a) Circuit used to simulate the hTron behavior in SPICE, identical to the one used in Figure 3 of [12]. The power dissipated in the heater increases the channel's temperature t_{Ch} , decreasing the channel switching current I_{SW} . As the channel switches to the normal phase, the bias current I_{Ch} is transferred to a 50Ω load R_{Load} , allowing the channel to reset back to the superconducting state. SPICE simulation result of the b) effective channel temperature and of the c) electrical behavior of the hTron device. The channel temperature and switching current were computed using Equation 1 and Equation 2, respectively. The device and simulation parameters were given by [12], while the model parameters $I_{\text{H,SUPP}}$ and $J_{\text{SW}}(T_{\text{SUB}})$ were extracted from the $I_{\text{SW}}(i_H)$ plots using our method presented in this work.

4 Model performance and comparison with previous attempt

In this section, we applied our parameter extraction method to heater-dependent switching current measurements from Figure 5 of Baghdadi et al. [12], successfully replicating the device behavior as shown in Figure 6. The measured device switching current at substrate temperature is approximately $J_{\text{SW}}(T_{\text{SUB}}) \simeq 120 \mu\text{A}$, and the $J_{\text{SW}}(i_H)$ curve does not present a plateau at low heater current.

Our model closely matches the measurements but slightly overestimates the measured $J_{\text{SW}}(T_{\text{SUB}})$. This discrepancy might be due to channel constriction. From their measurements, we extracted the parameters: $I_{\text{H,SUPP}} = 80.9 \mu\text{A}$ and $\hat{J}_{\text{SW}}(T_{\text{SUB}}) = 122.9 \mu\text{A}$. Applying our

method to the previous 3D electrothermal model results curve from Figure 5 of [12] resulted in $I_{H,SUPP} = 79.5 \mu\text{A}$ and $\hat{J}_{SW}(T_{SUB}) = 116.1 \mu\text{A}$, against the previous model that predicted $J_{SW}(T_{SUB}) = 113.9 \mu\text{A}$. We computed a retrapping current value of $I_R = 20.3 \mu\text{A}$ using the relation given in [27], which is comparable to Baghdadi et al.'s measured value of approximately $I_R \approx 21 \mu\text{A}$.

In our simulation (Figure 6a), the hTron, shunted by a 50Ω load and biased at $100 \mu\text{A}$, switches with a 1-ns heater pulse, diverting the current into the resistor. The channel then reverts to its superconducting state, allowing current return with a time constant determined by the channel inductance and load resistance. Notably, our SPICE simulation (Figure 6b and Figure 6c) doesn't account for the temperature rise from Joule heating when the channel is in the normal state. However, this effect is taken into account by our hotspot growth rate equation [27], which makes our model valid. The pulse and hotspot resistance, shown in Figure 6c, align with Baghdadi et al.'s results (Figure 3c [12]), validating our model.

In order to simulate the device transient behavior, we matched the device activation time with the one observed in Figure 3c of [12], estimate as $\tau_{on} \approx 750 \text{ ps}$. This gives an RC time constant of $\tau_{filter} = 1.6 \text{ ns}$ for the lumped-element sub-circuit that simulates heat transfer.

All simulation parameters used in [12] are listed here: $w_c = 600 \text{ nm}$, $w_h = 500 \text{ nm}$, channel inductance $L_{Ch} = 500 \text{ nH}$, $T_{SUB} = 3 \text{ K}$, $T_C = 8.4 \text{ K}$, NbN thickness $d_c = 20 \text{ nm}$, $R_{SHEET} = 470 \Omega/\square$. Note that the heater's thickness and resistance, embedded in our fitting parameters, are unused by our model.

Finally, we compared both models' execution speeds by running the published simplified 0D electrothermal model in SPICE, solving heat equations with behavioral sources as implemented by Castellani [21], and comparing it to our model in a 250ns-long simulation of the circuit described in Figure 6a. We have set the SPICE parameter `reltol` = 10^{-6} for both models, as suggested by El Dandachi [28], and gathered the simulation results in Table 1. In a first simulation run, we varied the maximum simulation timestep Δt_{max} from 1 ps to 10 ps over 11 steps, and our model took less than eleven seconds to run, while the previous model took eight hours. In a second run, we varied the maximum timestep from 1 fs to 50 ps across 48 steps, and our model took less than four hours to run, while the previous model had to be halted after two days because it was stuck at a significantly slow simulation speed in the order of $\approx 1 \text{ fs/s}$. At this speed, it would take almost 3 days to complete the 250 ns of simulation before setting a higher value of maximum timestep.

	Run 1: $\Delta t_{\max} = 1 \text{ ps...10 ps}$		Run 2: $\Delta t_{\max} = 1 \text{ fs...50 ps}$	
	# Time-points	Simulation Time	# Time-points	Simulation Time
Previous model	813,628	8.0 hours	N/A	N/A
Our model	2,045	10.8 seconds	1,189,652	3.3 hours

Table 1: Comparison of simulation speed between the previous model designed by Baghdadi et al. [12] and our model for the same SPICE circuit but different time resolutions.

To conclude, the enhanced simulation speed of our model can be mainly explained by two factors. First, the previous model required solving a greater number of nodes due to its approach of using behavioral sources to solve the heat transfer equations of the entire system. Second, unlike our model, it did not incorporate our enhanced hotspot integrator sub-circuit, potentially leading to a higher number of timepoints [28]. While our simulations were conducted on a personal computer, and performance can vary between different machines, our results are significant. We successfully reduced typical simulation times from hours to mere minutes or even seconds, making such simulations feasible in practice on a personal computer for the first time, opening the door for their widespread use.

5 Discussion

This section discusses the challenges of predicting weak spots in superconducting nanowires, the impact of hidden parameters in our model, and the prediction of the device activation delay and operating speed, highlighting both the strengths and limitations of our approach.

In the current state of research, accurately predicting the location and number of weak spots — or areas with reduced critical current — along a channel remains unfeasible. Weak spots located away from the heated area are responsible for the plateau, which is not part of the behavior of the device, but rather due to channel width-dependent effects arising from the fabrication process. Therefore, we choose to get rid of the plateau during the parameter extraction, effectively fitting to the linear part of the $J_{\text{SW}}(i_{\text{H}})$ plots. As a result, the ideal model $\hat{J}_{\text{SW}}(i_{\text{H}})$ is a hypothetical curve that probes the critical current directly below the heater, theoretically representing the channel's critical current as if there was no weak spots. The plateau can then be set to any constriction level J_{CONSTR} . While we observed that the plateau level is smaller for narrower channels, it cannot be accurately predicted due to its intrinsic stochastic nature. Locating and removing constrictions in superconducting nanowires would be beneficial both in photon detection and device operation.

Regarding the parameter η in Equation 1, we used the value of $\eta = 2$ in this paper based on its optimal fit with Baghdadi et al.'s measurement data [12]. However, Butters suggests $\eta = 3$ (See

Equation 3.30 of [23]), implying a stronger dependence of the channel temperature with the heater current. The value of $\eta = 3$ aligns more closely with our measurement data, especially when i_H is close to $I_{H,\text{SUPP}}$. However, our devices are severely constricted, showing a plateau in most cases. Thus more experimental data on less constricted devices would help determine the best value for η . While a more complicated equation could potentially better describe the channel temperature as a function of heater current, the strength of our approach lies in its simplicity: introducing an additional free parameter would counteract this benefit, making our model less straightforward without a substantial increase in predictive accuracy for our specific application.

In this study, the measured devices are from a single wafer, implying that some geometrical parameters such as the oxide thickness do not explicitly appear in the fitting equations, and are thus hidden. Consequently, new measurements and recalibration of the model's parameters would be required to predict the behavior of devices with a different oxide thickness. Even though the previous model does not present hidden parameters, its prediction capabilities are limited as well. Indeed, it contains various thermal parameters that are either extracted from literature or fitted from measurements, and cannot be predicted from geometry. In contrast, our high-level curve-fitting approach simplifies the analysis, allows for a systematic process of parameters extraction for any geometry, and outperforms the previous attempt in accuracy and speed.

Finally, the heat transfer from the heater to the channel through the oxide is a critical factor limiting the operating speed of the devices, resulting in a non-zero device activation delay, τ_{on} . In complicated circuits, this delay becomes an increasingly significant figure for circuit designers. Indeed, accurately predicting and simulating the maximum operating speed of a real-world circuit is essential. In our approach, we intentionally over-simplified the way we modeled the heat transfer, offering the advantage of only including one parameter — an RC time constant denoted τ_{filter} , which can be directly obtained from τ_{on} —, making it straight-forward to implement in practice. However, as seen in Figure 5, our model's prediction of the activation delay is limited for low input currents. At higher currents, though, our model accurately predicts the activation delay, allowing one to simulate the temporal behavior of a hTron-based circuit close to the maximum operating speed. As a final note, while the minimum measured activation delay is in the order of 1 ns to 10 ns for our particular device, it is noteworthy that the fabricated devices were not designed for speed. A thinner oxide layer, as well as narrower heater wires would greatly improve the reaction speed of hTron devices.

6 Conclusion

Our approach to modeling the hTron device relies on the fitting of simple physics-informed equations to a relatively large amount of experimental data. All the fitting parameters are extracted from basic measurements, and no arbitrary parameter has to be tuned to better fit our measurements. The static behavior was modeled from the critical current measurements performed on 17 hTrons having 9 different geometries. We were able to extract the two relevant fitting parameters, and extrapolate them for hTron geometries that were not measured. Moreover, we were able to simulate the hTron transient response over a large span of current inputs thanks to activation delay measurements — delay between the application of a heater current pulse and the switching of the channel. This transient behavior is critical in circuit design as it sets the maximum operating speed of a circuit. We applied our model on measurement data published by Baghadi et al. [12], and obtained a better agreement than their attempt. Moreover, we compared the simulation speed of both approaches on a personal computer in SPICE, and obtained a result in seconds, while the previous approach completed the same simulation in hours. Consequently, our model and SPICE implementation is tailored for efficient design iterations in nanowire-based electronics. Finally, our model effectively simulates devices for any constriction — or plateau — level, a critical feature given the unpredictability of these occurrences during circuit design.

Our findings corroborate the positioning of the hTron as an alternative to the nTron device for applications requiring both high output impedance and electrical isolation between gate and channel. In a broader view point, superconducting nanowires could complement Josephson Junctions in areas where they are currently lacking. Looking forward, we will use our model to solve larger and more complex circuit like SNSPD arrays readouts. The high simulation speed capability, accuracy, and simplicity of our approach positions this work as a promising first step for the building of useful simulation tools for nanowire-based circuits.

Acknowledgements

The initial stages of the research were sponsored by the U.S. Department of Energy, Office of Science, Office of Basic Energy Sciences, under Award Number DE-AC02-07CH11359. The completion of data analysis and presentation were sponsored by the National Science Foundation under Grant No. OMA-2137723. The authors thank Alessandro Restelli, Joshua Bienfang and Ilya Charaev for helpful scientific discussions. V.K. would like to thank Edoardo Charbon from the Advanced Quantum Architecture (AQUA) Laboratory at the Swiss Federal Institute of Technology (EPFL). O.M.

acknowledges support from the NDSEG Fellowship program. M. Colangelo acknowledges support from MIT Claude E. Shannon award.

References

- [1] Ladd, T.D., Jelezko, F., Laflamme, R., Nakamura, Y., Monroe, C., O'Brien, J.L.: Quantum computers. *nature* **464**(7285), 45–53 (2010)
- [2] Oripov, B.G., Rampini, D.S., Allmaras, J., Shaw, M.D., Nam, S.W., Korzh, B., McCaughan, A.N.: A superconducting-nanowire single-photon camera with 400,000 pixels. arXiv preprint arXiv:2306.09473 (2023)
- [3] Islam, M.M., Alam, S., Hossain, M.S., Roy, K., Aziz, A.: A review of cryogenic neuromorphic hardware. *Journal of Applied Physics* **133**(7) (2023)
- [4] Likharev, K.K.: In: Weinstock, H., Ralston, R.W. (eds.) *Rapid Single-Flux-Quantum Logic*, pp. 423–452. Springer, Dordrecht (1993). https://doi.org/10.1007/978-94-011-1918-4_14 . https://doi.org/10.1007/978-94-011-1918-4_14
- [5] Soloviev, I.I., Klenov, N.V., Bakurskiy, S.V., Kupriyanov, M.Y., Gudkov, A.L., Sidorenko, A.S.: Beyond moore's technologies: operation principles of a superconductor alternative. *Beilstein journal of nanotechnology* **8**(1), 2689–2710 (2017)
- [6] McCaughan, A.N., Berggren, K.K.: A superconducting-nanowire three-terminal electrothermal device. *Nano letters* **14**(10), 5748–5753 (2014)
- [7] Zheng, K., Zhao, Q.-Y., Lu, H.-Y.-B., Kong, L.-D., Chen, S., Hao, H., Wang, H., Pan, D.-F., Tu, X.-C., Zhang, L.-B., *et al.*: A superconducting binary encoder with multigate nanowire cryotrons. *Nano Letters* **20**(5), 3553–3559 (2020)
- [8] Huang, Y.-H., Zhao, Q.-Y., Chen, S., Hao, H., Wang, H., Guo, J.-W., Tu, X.-C., Zhang, L.-B., Jia, X.-Q., Chen, J., *et al.*: Splitter trees of superconducting nanowire cryotrons for large fan-out. *Applied Physics Letters* **122**(9) (2023)
- [9] Zhao, Q.-Y., McCaughan, A.N., Dane, A.E., Berggren, K.K., Ortlepp, T.: A nanocryotron comparator can connect single-flux-quantum circuits to conventional electronics. *Superconductor Science and Technology* **30**(4), 044002 (2017)

[10] Toomey, E., Onen, M., Colangelo, M., Butters, B., McCaughan, A., Berggren, K.: Bridging the gap between nanowires and josephson junctions: a superconducting device based on controlled fluxon transfer. *Physical review applied* **11**(3), 034006 (2019)

[11] McCaughan, A.N., Verma, V.B., Buckley, S.M., Allmaras, J., Kozorezov, A., Tait, A., Nam, S., Shainline, J.: A superconducting thermal switch with ultrahigh impedance for interfacing superconductors to semiconductors. *Nature electronics* **2**(10), 451–456 (2019)

[12] Baghdadi, R., Allmaras, J.P., Butters, B.A., Dane, A.E., Iqbal, S., McCaughan, A.N., Toomey, E.A., Zhao, Q.-Y., Kozorezov, A.G., Berggren, K.K.: Multilayered heater nanocryotron: A superconducting-nanowire-based thermal switch. *Physical Review Applied* **14**(5), 054011 (2020)

[13] Zheng, K., Zhao, Q.-Y., Kong, L.-D., Chen, S., Lu, H.-Y.-B., Tu, X.-C., Zhang, L.-B., Jia, X.-Q., Chen, J., Kang, L., *et al.*: Characterize the switching performance of a superconducting nanowire cryotron for reading superconducting nanowire single photon detectors. *Scientific reports* **9**(1), 16345 (2019)

[14] Buzzi, A., Castellani, M., Foster, R.A., Medeiros, O., Colangelo, M., Berggren, K.K.: A nanocryotron memory and logic family. *Applied Physics Letters* **122**(14) (2023)

[15] Butters, B.A., Baghdadi, R., Onen, M., Toomey, E.A., Medeiros, O., Berggren, K.K.: A scalable superconducting nanowire memory cell and preliminary array test. *Superconductor Science and Technology* **34**(3), 035003 (2021)

[16] Oripov, B., Rampini, D., Allmaras, J., Shaw, M., Nam, S.W., Korzh, B., McCaughan, A.: Thermally coupled imager with 400,000 pixels (2023)

[17] Zheng, K., Zhao, Q.-Y., Lu, H.-Y.-B., Kong, L.-D., Chen, S., Hao, H., Wang, H., Pan, D.-F., Tu, X.-C., Zhang, L.-B., *et al.*: A superconducting binary encoder with multigate nanowire cryotrons. *Nano Letters* **20**(5), 3553–3559 (2020)

[18] Foster, R.A., Castellani, M., Buzzi, A., Medeiros, O., Colangelo, M., Berggren, K.K.: A superconducting nanowire binary shift register. *Applied Physics Letters* **122**(15) (2023)

[19] Castellani, M., Medeiros, O., Foster, R.A., Buzzi, A., Colangelo, M., Bienfang, J.C., Restelli, A., Berggren, K.K.: A nanocryotron ripple counter integrated with a superconducting nanowire single-photon detector for megapixel arrays. *arXiv preprint arXiv:2304.11700* (2023)

[20] Shainline, J.M., Buckley, S.M., McCaughan, A.N., Chiles, J.T., Jafari Salim, A., Castellanos-Beltran, M., Donnelly, C.A., Schneider, M.L., Mirin, R.P., Nam, S.W.: Superconducting optoelectronic loop neurons. *Journal of Applied Physics* **126**(4) (2019)

[21] Castellani, M.: Design of superconducting nanowire-based neurons and synapses for power-efficient spiking neural networks. Master's thesis, Politecnico di Torino (2020)

[22] Dane, A.E., McCaughan, A.N., Zhu, D., Zhao, Q., Kim, C.-S., Calandri, N., Agarwal, A., Bellei, F., Berggren, K.K.: Bias sputtered nbn and superconducting nanowire devices. *Applied Physics Letters* **111**(12) (2017)

[23] Butters, B.A.: Digital and microwave superconducting electronics and experimental apparatus. PhD thesis, Massachusetts Institute of Technology (2022)

[24] Lin, S.-Z., Roy, D.: Role of kinetic inductance in transport properties of shunted superconducting nanowires. *Journal of Physics: Condensed Matter* **25**(32), 325701 (2013)

[25] Kundert, K.: The Designer's Guide to Spice and Spectre. Kluwer Academic Publishers, Boston (2003)

[26] Medeiros, O., Colangelo, M., Charaev, I., Berggren, K.K.: Measuring thickness in thin nbn films for superconducting devices. *Journal of Vacuum Science & Technology A* **37**(4) (2019)

[27] Berggren, K.K., Zhao, Q.-Y., Abebe, N., Chen, M., Ravindran, P., McCaughan, A., Bardin, J.C.: A superconducting nanowire can be modeled by using spice. *Superconductor Science and Technology* **31**(5), 055010 (2018)

[28] El Dandachi, T.: Efficient simulation of large-scale superconducting nanowire circuits. Master's thesis, Massachusetts Institute of Technology (2023)

[29] Charaev, I., Silbernagel, T., Bachowsky, B., Kuzmin, A., Doerner, S., Ilin, K., Semenov, A., Roditchev, D., Vodolazov, D.Y., Siegel, M.: Proximity effect model of ultranarrow nbn strips. *Physical Review B* **96**(18), 184517 (2017)

[30] Kerman, A.J., Dauler, E.A., Yang, J.K., Rosfjord, K.M., Anant, V., Berggren, K.K., Gol'tsman, G.N., Voronov, B.M.: Constriction-limited detection efficiency of superconducting nanowire single-photon detectors. *Applied Physics Letters* **90**(10) (2007)

[31] Colangelo, M., Walter, A.B., Korzh, B.A., Schmidt, E., Bumble, B., Lita, A.E., Beyer, A.D., Allmaras, J.P., Briggs, R.M., Kozorezov, A.G., *et al.*: Large-area superconducting nanowire single-photon detectors for operation at wavelengths up to $7.4\ \mu\text{m}$. *Nano Letters* **22**(14), 5667–5673 (2022)